Aperture Mask Interferometry with an Integral Field Spectrograph

Neil Zimmerman[a,b], Anand Sivaramakrishnan[c,b,d], David Bernat[e], Ben R. Oppenheimer[b], Sasha Hinkley[f,g], James P. Lloyd[e], Peter Tuthill[h], Douglas Brenner[b], Ian R. Parry[i], Michal Simon[d], John E. Krist[j], Laurent Pueyo[k,g]

[a] Max Planck Institute for Astronomy, Königstuhl 17, 69117 Heidelberg, Germany,

[b] Department of Astrophysics, American Museum of Natural History, 79th Street at CPW, New York, NY 10024, USA

[c] Space Telescope Science Institute, 3700 San Martin Drive, Baltimore, MD 21218, USA

[d] Department of Physics and Astronomy, Stony Brook University, Stony Brook, NY 11794, USA

[e] 230 Space Sciences Building, Cornell University, Ithaca, NY 14853, USA

[f] California Institute of Technology, Pasadena, CA 91125, USA

[g] Sagan Fellow

[h] School of Physics, University of Sydney, NSW 2006, Australia

[i] Institute of Astronomy, University of Cambridge, Cambridge CB3 OHA, UK

[j] Jet Propulsion Laboratory, Pasadena, CA 91109, USA

[k] Department of Physics & Astronomy, Johns Hopkins University, 366 Bloomberg Center, 3400 N. Charles Street, Baltimore, MD 21212, USA

ABSTRACT

A non-redundant pupil mask placed in front of a low-resolution integral field spectrograph (IFS) adds a spectral dimension to high angular resolution imaging behind adaptive optics systems. We demonstrate the first application of this technique, using the spectroscopic binary star system β CrB as our target. The mask and IFS combination enabled us to measure the first low-resolution spectrum of the F3–F5 dwarf secondary component of β CrB, at an angular separation 141 mas from its A5–A7Vp primary star. To record multi-wavelength closure phases, we collected interferograms simultaneously in 23 spectral channels spanning the J and H bands (1.1 μm–1.8 μm), using the Project 1640 IFS behind the 249-channel PalAO adaptive optics system on the Hale telescope at Palomar Observatory. In addition to providing physical information about the source, spectrally-resolved mask fringes have the potential to enhance detection limits over single filter observations. While the overall dynamic range of our observation suffers from large systematic calibration errors, the information gleaned from the full channel range improves the dynamic range by a factor of 3 to 4 over the best single channel.

Further author information: (Send correspondence to N.Z. E-mail: zimmerman@mpia.de

Optical and Infrared Interferometry III, edited by Françoise Delplancke, Jayadev K. Rajagopal, Fabien Malbet,
Proc. of SPIE Vol. 8445, 84452G · © 2012 SPIE · CCC code: 0277-786/12/$18 · doi: 10.1117/12.926204

1. INTRODUCTION

Non-redundant aperture masking interferometry[1–4] overcomes speckle noise-imposed limits[5,6] imposed on high-resolution diffraction-limited imaging in the infrared. The telescope pupil is obstructed by a non-redundant mask (NRM), which alters the point spread function from a classical Airy disk to a pattern of interference fringes (an interferogram). Certain properties of this interferogram, most notably its associated set of closure phases, are robust to perturbations that corrupt a conventional filled-aperture image. Sub-apertures in the pupil mask are analogous to the antennas of a radio interferometer, with the quadratic detection of energy by a focal plane array replacing the numerical correlator of radio astronomers. Indeed, the concept of closure phase calibration was developed for multiple-antenna radio telescopes decades before being applied at optical and infrared wavelengths.[7] In the case of a *non-redundant* aperture mask, the baseline between any pair of subapertures in the mask is unique. Consequently, each fringe in the interferogram is unambiguously identified with the baseline that produced it. Under appropriate conditions, closure phases depend only on the geometry of the sub-aperture layout and the intensity distribution of the target. The net result is that the sparse aperture mask observer trades a flood of degraded observables for a small number of well-calibrated ones.

Necessarily, there are trade-offs between NRM and traditional full-aperture imaging. NRM is preferred mostly in the regime of high dynamic range measurements on angular scales near the diffraction limit of the telescope. Even in this regime the benefits of aperture masking interferometry rest delicately on the strategy of data acquisition. In the near-infrared, rapid and severe changes in the wave front error caused by atmospheric instabilities set a time scale on the order of 10-100 milliseconds. Without active wave front correction, an aperture mask observer has to "freeze" the effects of atmospheric aberrations in order to utilize the interferograms' closure phases with useful accuracy (less than $\sim$1 radian). Nonetheless, by combining a large ensemble of very short exposures, major discoveries of otherwise inaccessible astrophysical sources have been made, such as the resolved structure of dust envelopes and nebulae around evolved stars,[8–10] and accretion phenomena in interacting binary star systems.[11]

Over the last decade, observational work by the high-contrast imaging community has shown that when using a high-order adaptive optics system under excellent seeing conditions, the dominant errors in the image plane are caused by the long-lived, non-common path errors originating from telescope and instrument optics, rather than atmospheric distortions.[12] In a conventional full-aperture image these systematic aberrations, even after correction by an adaptive optics (AO) system, result in a halo of quasi-static speckles around the target star.[5,6,13–16] Aperture mask observations can take advantage of the same AO correction to boost their integration times, which are no longer limited by the atmospheric coherence time.[17] Furthermore, the closure phases should be largely immune to the non-common path errors that form speckles. When aperture masking is performed after wave front corection by an AO system, wave front distortions are compensated to such an extent that closure phase precision remains stable over more than ten minutes to within one degree.[18,19] This is an order of magnitude improvement over what is possible with the extremely short (< 0.1 s) exposures necessary to "freeze" the fringe phase without AO under good seeing conditions.[1–3] The longer integration times enabled by high-order AO have opened up the possibility of using the technique to search for faint companions at extremely close angular separations from nearby stars. In practice, the inner working angle of a Lyot coronagraph, the most widely used tool for high-contrast imaging, is $\sim 3\lambda/D$.[12,20–23] For a star at 50 pc observed in H band on a 5-meter telescope, for example, this implies that the lower limit of orbital separation that can be probed is $\sim$ 10AU. Aperture masking observations, however, reach smaller angular separations, near the telescope diffraction limit, thereby complementing coronagraphic surveys and probing scientifically valuable parameter space.

In recent years a number of promising results have been attained by combining non-redundant aperture mask (NRM) interferometry with AO correction. Besides unique resolved measurements of individual binary and multiple star systems,[18,24,25] there has been one high-contrast survey of stars in the Upper Scorpius moving group,[26] and another survey for companions of L-dwarfs.[27] A large portion of the first survey and all of the latter survey were carried out at with the Palomar Hale Telescope's adaptive optics system (PALAO) in the near-infrared.[28] Both have yielded new sub-stellar companion candidates. Hinkley et al. used L'-band masking with the NIRC2 camera at Keck Observatory to place constraints on planetary mass companions within the orbital radius of those already detected through direct imaging.[29–33] More recently, NRM+AO observations have revealed several low- and planetary-mass companions residing in the inner gaps of transitional disks.[34–36]

We extend the NRM technique to integral field spectroscopy behind an AO system, thereby adding a wavelength dimension to the closure phase data set. The Project 1640 (P1640) integral field spectrograph on the Palomar Hale Telescope was designed to implement an apodized Lyot coronagraph to carry out a survey for young, giant, long-period exoplanets.[20,21,37] The coronagraph forms an image on a microlens array at the spectrograph entrance. From there, the beam from each microlens is dispersed by a prism and focused as a low-resolution spectrum on the detector. For more details on the P1640 design, see Hinkley et al.;[37] for the original description of a microlens-based integral field spectrograph (IFS), see Bacon et al.[38,39]

The spectral information provided by the IFS serves two functions in P1640's standard survey mode. First, the chromatic diversity allows the observer to disentangle quasi-static speckles—whose positions scale radially from the star as a function of wavelength—from true faint sources, and hence limit their effect on the overall dynamic range.[40,41] Second, the low-resolution spectrum ($\sim$ 70 nm resolution spanning the J and H bands) acquired for each spatial element enhances the characterization of any detected source beyond conventional broadband photometry.[42,43]

We had similar motivations behind our demonstration combining NRM interferometry with the P1640 IFS. First, the dynamic range achieved by combining closure phases from multi-channel interferograms may exceed that reached in the usual single-filter case. This application has been suggested,[44] but not implemented until our observations. Second, as in the case of the coronagraph mode, a companion spectrum retrieved by an IFS would place useful constraints on its mass, temperature, and possibly composition. A successful example of spectrum extraction from IFS aperture mask data would provide a useful template for more ambitious targets.

We tested our approach with an observation of the well-studied 10.5 yr-period spectroscopic binary β CrB (HD 137909; $V = 3.7^{\rm m}$; J2000 coordinates $\alpha = 15^{\rm h}27^{\rm m}49.731^{\rm s}, \delta = +29°06'20.53''$; d = 35.0 pc).[45] The primary component of β CrB is an oscillating, chemically peculiar A star with strong magnetic features.[46] Its F-dwarf companion was first discovered in 1907 through radial velocity measurements.[47] Muterspaugh et al. carried out the most recent orbit determination, combining nearly one century of radial velocity data with astrometry from the Palomar High-precision Astrometric Search for Exoplanet Systems (PHASES) project and speckle imaging.[48] The projected semi-major axis of the binary orbit is 204 mas; at our observation epoch their angular separation was 141 mas, close to twice the Hale Telescope diffraction limit in the H band. The contrast ratio between the primary and secondary is roughly a factor of four across the J and H bands.

2. OBSERVATIONS AND CLOSURE PHASE EXTRACTION

Using design parameters similar to previous pupil masks behind PALAO, we ordered the fabrication of a nine-hole non-redundant mask pattern on a thin stainless steel disk. The mask geometry was scaled to match the pupil plane in the P1640 coronagraph, at the position of the Lyot stop. Each subaperture in the mask is a hexagon of point-to-point diameter 0.403 mm (measured across opposing vertices), translating to 0.526 m in the telescope pupil (compared to the 5.08 meter primary mirror aperture). The shortest and longest effective baselines on the mask are 0.76 m and 4.23 m. The overall transmission of the mask is 9.1% of the full telescope pupil.

We configured P1640 for NRM observations on 2010 March 24 by replacing the coronagraph Lyot stop mask with the non-redundant pupil mask. Once the pupil mask was mounted, the only change necessary from normal coronagraph data acquisition was to ensure that the target was offset from the focal plane mask, effectively a 370 mas-diameter occulting spot near the center of the 3.8″-wide field of view of the IFS. With the mask in place, we acquired 16 non-destructive read (NDR) sequences of the interferogram of β CrB, the spectroscopic binary target. Each NDR sequence from our HAWAII-2 detector consisted of 20 successive 7.721 s reads, resulting in a total exposure time of 2471 s, about 41 minutes (more information on our detector read scheme can be found in Zimmerman et al.[49]).

We followed the target observation with a similar observing sequence of a nearby calibrator star κ CrB (HD 142091), with a slightly shorter integration time of 15 NDR sequences. Ten minutes separated the end of the last β CrB NDR sequence from the start of the first κ CrB NDR sequence. Both the target and calibrator stars were bright enough ($V = 3.7^{\rm m}$ and $4.8^{\rm m}$, respectively) to be acquired as natural guide stars by the Palomar AO system. Our log indicates $\sim$1″ seeing through the duration of this data set. The dates and exposure schemes of the observations are summarized in Table 1.

Target	Mean UT date	Air Mass	# of NDR sequences	# of reads	Total exposure time (s)
β CrB	2010 March 24 12:05	1.03	16	320	2471 s
κ CrB	2010 March 24 12:59	1.06	15	300	2316 s

Table 1. Summary of P1640 NRM observations

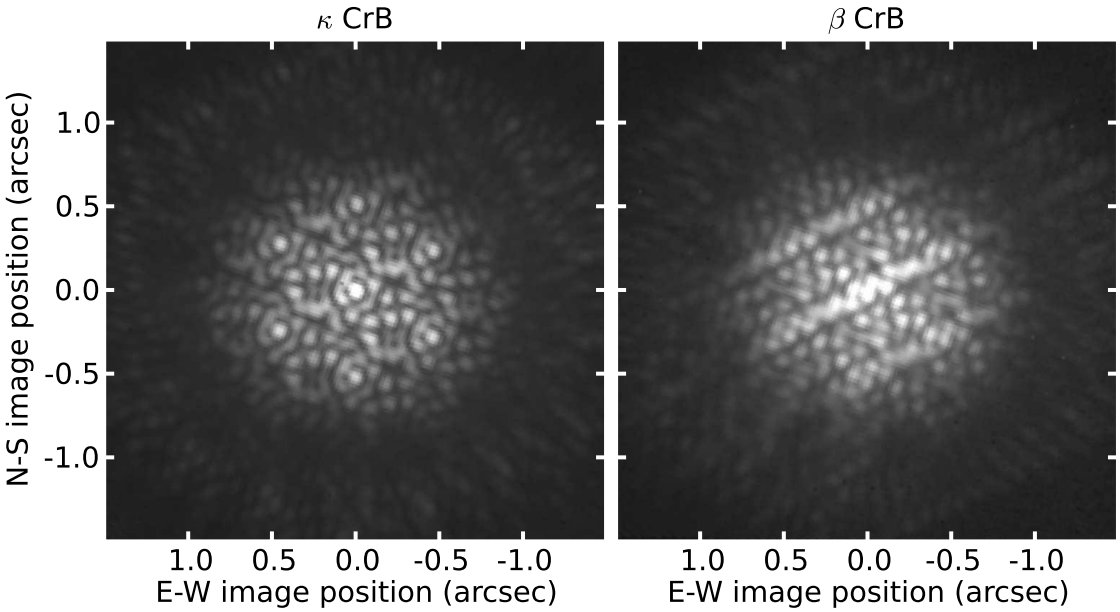

Figure 1. One example of an interferogram cube slice for each target: the calibrator κ CrB on the left and the spectroscopic binary β CrB on the right. Channel 21 of 23 (1.7 μm) is displayed, with a square-root stretch. For clarity, the cube channel images have each been cropped to center the brightest portion of the interferograms.

In NRM observations, it is typical to observe a single star as a calibration reference to measure systematic errors in the closure phases. We note that κ CrB in fact hosts a giant exoplanet candidate with projected semi-major axis 87 mas, as inferred from Doppler measurements.[50,51] However, given the planet's mass and and the estimated system age—2.0 $M_{\rm Jup} \sin i$ and 2.5 Gyr, respectively—it is highly unlikely that emission from this object could have produced a measurable change in the source wave front of κ CrB. Suppose the orbital inclination of the exoplanet candidate is only 1 deg, so that mass is actually 100 $M_{\rm Jup}$. Then, according to the cooling curves for low-mass stars by Baraffe et al.,[52] at an age of 1 Gyr, in H band, it would appear at a contrast of ~ 10 magnitudes with respect to the host star. While 10 magnitudes of contrast is a plausible goal for high-contrast NRM observations to reach in the near future, it is well beyond the performance we achieve in this experiment, in terms of both measurement precision and calibration of systematic errors. Therefore, we confidently treat our κ CrB data as those of an ideal point source.

We used the Project 1640 Cube Extraction Pipeline (PCXP) to translate our raw dispersed fringe data into cubes. This software is fully described in Zimmerman et al.;[49] a finished cube consists of 23 channel images spanning the 1.10 μm—1.76 μm passband. The pixels in the cube are indexed by three coordinates: two spatial indices, and one wavelength index. Each pair of spatial indices corresponds to one *spaxel*, an element in the 200×200 microlens array at the spectrograph entrance. We show one example of the long exposure interferograms of each target in Figure 1.

We sent the interferogram cubes created by the PCXP through a separate customized pipeline written in Python/NumPy, producing a complex visibility data cube (amplitude and phase) for each interferogram. Our NRM pipeline also applies an algorithm to compensate for cross-talk between neighboring spectra in the IFS focal plane. Next, we extracted the fringe phases from each Fourier-domain cube slice. Each slice (indexed by exposure and channel) yields 84 closure phases—one for each of the $\binom{9}{3}$ possible triangles among the nine sub-apertures. Of these, 28 closure phases are independent measurements, since a given baseline reappears in

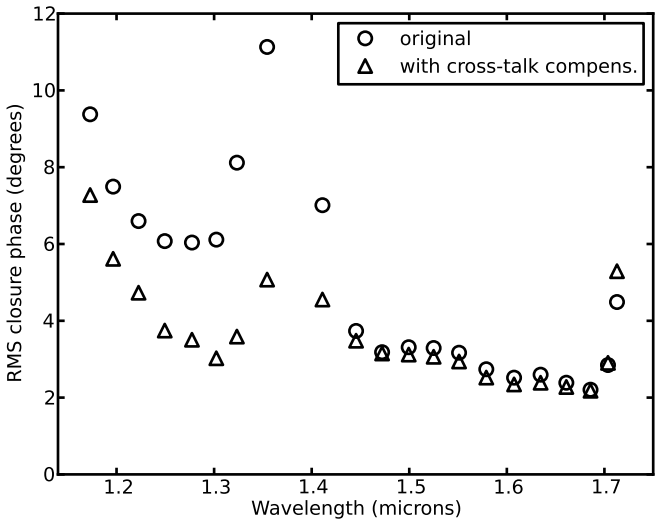

Figure 2. RMS closure phase values in one long calibration exposure, with and without cross-talk compensation. When we do not account for cross-talk, the visibility phasors are corrupted by scaled-down, shifted "ghost" phasors from offset channels.

many triangles.

3. STATISTICAL PROPERTIES OF THE SPECTRALLY-RESOLVED CLOSURE PHASES

The ability of NRM observations to reach high dynamic range is dependent on the stability and accuracy of the extracted closure phases. Much can be learned about our unique data set by analyzing the stochastic behavior of the calibrator closure phases alone. In Figure 2, we show the root mean square (RMS) value of the closure phases in one calibrator (κ CrB) exposure as a function of wavelength. We compared the results of extraction both with and without cross-talk compensation applied to the original visibility data cube. Ideally, the closure phases for a point source would be zero. However, it is normal in AO NRM observations for systematic errors, likely due to non-common path phase errors that deviate from the piston phase error model, to cause slight offsets to individual closure phases.[26,29] One of the purposes of acquiring a calibration star alongside the NRM target is to subtract this instrumental component. Since the AO wave front correction degrades towards shorter wavelengths, we expect that the errors would be slightly higher in the J band, which is in fact the case. Another cause of better performance at longer wavelengths is the fact that the interference fringes were oversampled at longer wavelengths, making them less susceptible to errors in cube extraction. The longest baseline (4.23 m) fringe is sampled at 2.3× the Nyquist rate at the red end of the passband ($\lambda = 1.76$ μm), versus only 1.4× the Nyquist rate at the blue end of the cube ($\lambda = 1.10$ μm).

It is also apparent that independent of these effects, the deviations from zero closure phase are to some extent anti-correlated with interferogram signal-to-noise ratio. The water absorption trough around 1.4 μm (in between the J and H bands) coincides with a bump in κ CrB's RMS closure phase, notably attenuated by the cross-talk compensation algorithm. At channels near the edges of the passband, both water absorption and the transmission function of the instrument blocking filter lower the signal.

We tabulate RMS values and scatter of various subsets of our closure phase data in Table 2. Here, the column marked "Std. dev." represents the typical scatter within a closure phase measurement rather than the scatter between different closure phases. To calculate this, we determined the time series standard deviation of each closure phase. The average of these standard deviations among all closure phases within the specified channel range are tabulated. It is encouraging that the typical standard deviation is below the RMS, since that suggests that the ensemble of measurements for each closure triplet does in fact provide a meaningful measure of the

Data set	Channel range	RMS (deg)	Std. dev. (deg)
κ	3–10	4.9	3.1
κ	11–22	3.0	1.6
β	3–10	23	7.3
β	11–22	25	3.9

Table 2. Root mean square and standard deviation values of closure phase data. Each listed standard deviation is the mean of the time series standard deviations of all closure phases in the set.

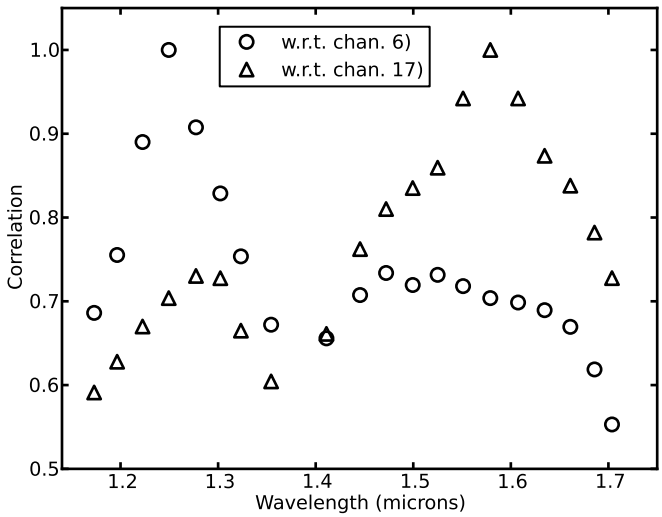

Figure 3. The cross-channel correlation of closure phase errors in the short exposure κ CrB data set, evaluated with respect to channel 6 and channel 17.

underlying systematic component. However, we note that our closure phases were in general not quite as stable as those acquired in previous AO NRM observations at Palomar. Lloyd et al., for example, measured a typical closure phase scatter of 0.6 deg at H band, for a fainter star than either of our targets.[18]

We are also interested in the cross-channel correlation of the closure phase variations, which is an indication of the statistical independence of the data cube channels. Let us represent the closure phase with triplet index q ($0 \leq q < N_{\rm trip}$) recorded in channel index w ($0 \leq w < N_{\rm chan}$) by $\Psi_{q,w}$. The correlation coefficient between the errors in a given closure phase q at two channels w_1 and w_2 is defined as follows:

$$\mathrm{Corr}\,(q, w_1; q, w_2) = \frac{\left\langle \left(\Psi_{q,w_1} - \overline{\Psi}_{q,w_1}\right)\left(\Psi_{q,w_2} - \overline{\Psi}_{q,w_2}\right)\right\rangle}{\sigma_{\Psi_{q,w_1}}\sigma_{\Psi_{q,w_2}}} \tag{1}$$

Here $\overline{\Psi}$ is the sample mean, and σ_Ψ is the sample standard deviation. Then, to quantify the independence of two channels of closure phase data w_1 and w_2, we can average $\mathrm{Corr}\,(q, w_1; q, w_2)$ over all triplets:

$$\overline{\mathrm{Corr}}(w_1; w_2) = \frac{\sum_{q=0}^{N_{\rm trip}-1} \mathrm{Corr}(q, w_1; q, w_2)}{N_{\rm trip}} \tag{2}$$

To see how the cross-channel correlation behaves with respect to one channel, we held the first channel index w_1 fixed and evaluated $\overline{\mathrm{Corr}}(w_1; w_2)$ across the passband for each w_2. In Figure 3 we show the results of this calculation, first with channel 6 (1.25 μm) fixed and then channel 17 (1.58 μm). As expected, in each case the function peaks at unity in the reference channel, since in that case both the numerator and denominator of the

	Separation (mas)	Position angle (deg. E of N)
Predicted	141.2	121.7
Measured	140.4 ± 0.6	119.22 ± 0.25

Table 3. Comparison between measured position offset of β CrB B with that predicted from the orbit by.[48]

expression in Equation 1 reduce to the variance of a given closure phase. What is important, however, is the high degree to which the closure phase errors are correlated across wavelength: between the middles of J and H band the correlation remains above 0.7. This is somewhat expected, since a non-common path error associated with some path length difference would perturb the phase over the entire wavelength range. We assess the impact of our measured closure phase variance and covariance values on detection limits in §5.

4. RESULTS OF THE β CRB CLOSURE PHASE MODEL

For both targets, we formed a mean closure phase set by averaging the extracted long exposure closure phases over time, and discarding the end channels due to their poor quality. Next, we subtracted the mean κ CrB closure phase set from the mean β CrB closure phase set, to remove systematic errors presumably present in both data sets. From here, we fitted a binary star model to the β CrB data in two stages, following an approach similar to that of Ireland et al. and Bernat et al.[24,27] First, we performed a "brute force" search over a coarse parameter grid. We explore a range of three parameters: radial separation (r), position angle (θ), and contrast (η). Although we expected η to vary with wavelength, for efficiency we initially treated it as a constant across the passband.

We evaluated binary star parameters using a maximum likelihood formulation (for a helpful overview, see Sivia[53]). To evaluate the misfit statistic of a given parameter combination, we took the sample covariance matrix of the closure phase data set into account, rather than treating the closure phases as statistically independent observables. This was necessary for two reasons: (i) the full set of 84 closure phases in a given channel is not linearly independent, and (ii) there are correlations in errors across channels, as shown previously in §3.

In the first outcome, the root-mean-square level of fit residuals between the best binary model and the calibrated closure phase measurements was 8.6 degrees. We found that a small subset of closure triangles were responsible for the majority of these systematic errors. We excluded the worst 15 of the 84, so that the remaining residuals in the peak J and H channels were all under 10 degrees. Repeating the full fitting procedure with the 69 retained closure phases recorded in 20 channels, the RMS fit residual decreased to 4.5 degrees. However, the change in the binary star solution was only marginal, probably because the flagged closure phases had already been weighted down due to high variances.

In Table 3, we list the position of the companion we recovered, alongside the expected one based on the established orbit.[48] The error bars on the best-fit r and θ values are based on the shape of the two-dimensional p.d.f. computed with the contrast ratio vector fixed. We found this p.d.f. to be nearly symmetric, and used the widest axis, 0.6 mas, as the error in both the radial and azimuthal directions. The overall disparity in position is only 6.2 mas, similar to the disagreement that Bruntt et al.[54] found in their AO-resolved direct imaging of the system (although they were comparing their position with the older orbit from Tokovinin[55]).

To derive spectra for the two stellar components of β CrB, we combined the solved contrast ratio function $\eta(\lambda)$ with total flux measurements of the interferograms. Since a near-infrared spectrum of κ CrB is included in the IRTF Spectral Library,[56] it was straightforward to calibrate the total channel fluxes of the β CrB data. The resulting pair of spectra are plotted in Figure 4, normalized to the mean flux density of the primary (A). We use a second plot, Figure 5, to clearly display the spectrum of the companion by itself. The error bars in the flux points are based on scaled parameter variances returned by the fitting algorithm, propagated through the calibration steps.

Recently, Bruntt et al.[54] carried out a detailed investigation into the physical properties of β CrB. They measured broadband fluxes from AO imaging with VLT/NACO and stellar diameters by long baseline optical interferometry with the CHARA Array. Combining those data sets, they arrive at effective temperature estimates

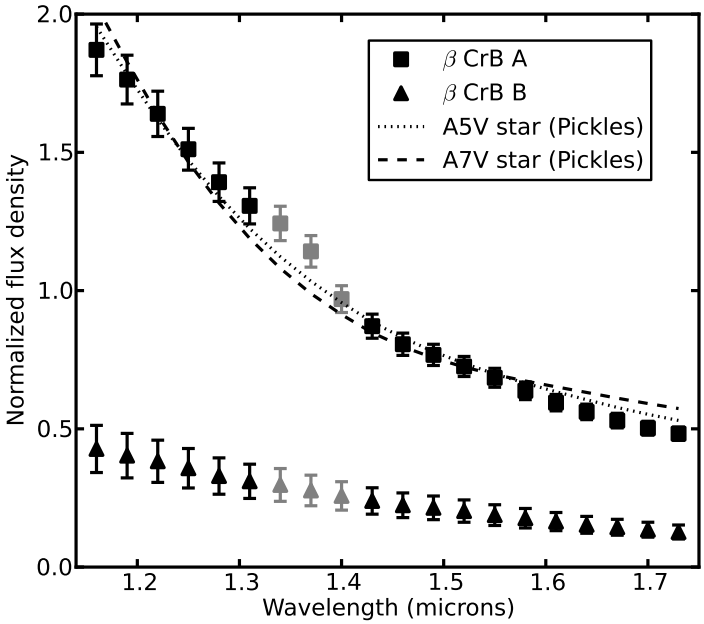

Figure 4. Spectra of β CrB A and β CrB B, normalized to the mean flux of β CrB A. We compare the spectrum of component A to two reference A-dwarf stars from the Pickles Atlas.[57] The gray shading indicates channels whose flux calibration was corrupted by variable telluric water absorption.

of 7980 ± 180 K and 6750 ± 230 K for the two stars. These temperatures imply spectral types in the range A5V–A7V and F2V–F5V.[58] We overplotted reference spectra in Figures 4 and 5 to confirm these results in our NRM data. For the secondary, we compared F3V and F5V spectrum examples from the IRTF Spectral Library. However, due to the lack of a sample of A stars in the IRTF library, we instead collected two appropriate reference spectra from the Pickles Atlas.[57] In each case, we smoothed the reference spectrum to the P1640 data cube resolution, using the procedure described in Zimmerman et al.[49] In both cases, we found a fair match with the spectral types of Bruntt et al. Surprisingly, the match for the secondary is closer than the primary's, even though the flux data points of the latter spectrum were less sensitive to errors in the closure phase model. Most of the disparity in the primary spectrum is in points susceptible to the telluric water absorption band between the J and H photometric bands. These points are distinguished in the plot by gray shading. Presumably, it is by mere chance that the flux calibration errors skewed in such a way that the F-dwarf spectrum remains smooth across the telluric channels.

5. DYNAMIC RANGE ESTIMATION

Commonly, the dynamic range of an optical interferometry observation is estimated by applying a Monte Carlo method to an empirical noise model.[59] In the case of AO-assisted NRM observations of relatively bright targets, detection limits are typically set by systematic errors in closure phase calibration rather than measurement scatter.[26,29] Therefore it is not surprising that in our experiment the uncalibrated systematic error components dominated the uncertainty in our deduction of the target source distribution. We know this is the case because the binary model fit residuals exceeded the uncertainties in the closure phase means implied by the statistics listed in Table 2.

In order to build a complete model of the systematic noise, we would need to observe multiple calibrator stars to reveal the variances and covariances associated with this error component within and across the spectrograph channels. The correlations seen in Section §3 among the stochastic closure phase variations suggest that there are also strong correlations between underlying systematic errors, which would ultimately affect the detection

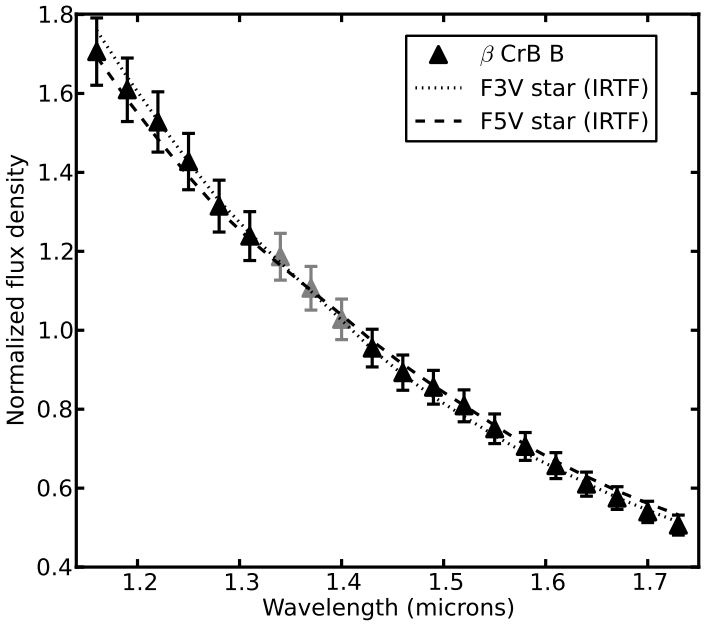

Figure 5. Mean-normalized spectrum of β CrB B measured from P1640 NRM data. We overplot the spectra of two F-dwarf stars from the IRTF Spectral Library: HD 26015 (F3V) and HD 27524 (F5V).

Wavelength subset	Sep. 33 mas–100 mas	Sep. 100 mas–166 mas
1.25 μm (chan. 6)	14:1	17:1
1.58 μm (chan. 17)	10:1	19:1
1.16 μm–1.73μm (chan. 3–22)	47:1	64:1

Table 4. Contrast ratios of the strongest spurious point source signals in the β CrB NRM data. The contrast ratios are given for two zones of separation from the primary star. For reference, 66 mas corresponds to λ/D for the Hale Telescope at 1.6 μm.

limits. Since we were only able to observe one calibrator star for this data set, we assess our sensitivity with an alternative approach.

Rather than measuring detection limits from simulated data sets, we treat the amplitudes of spurious χ^2 valleys in the β CrB source model as proxies for dynamic range. Assuming no true tertiary sources in the field are detectable in our β CrB data data set, the brightest false alarm revealed by a three source parameter grid search provide a measure that we expect to be roughly proportional to the detection limit. Although this does not provide a conventional detection limit, it at least allows us to quantitatively grasp how the sensitivity improves with the ensemble of spectrograph channels versus the single filter case.

We carried out a three source grid search on the calibrated β CrB closure phase data, with the parameters describing the known F-dwarf companion fixed at their best-fit values from Section §4. For the hypothetical tertiary source we tested a finely sampled range of positions inside two zones of separation centered on the primary star. The inner test annulus spanned separations between 33 mas and 99 mas ($0.5\lambda/D$–$1.5\lambda/D$ at 1.6 μm where D is the 5 m Hale Telescope aperture) and the outer annulus spanned angular separations 99 mas to 165 mas ($1.5\lambda/D$–$2.5\lambda/D$ at 1.6 μm). We determined the brightest proposed source within each annulus that *reduced* the χ^2 misfit statistic as compared to the best-fit binary model. The misfit statistic was computed separately for the single 1.25 μm data cube channel, the 1.58 μm data cube channel, and the 20-channel closure phase ensemble. For simplicity, we fixed the tertiary source model contrast ratio across the passband when calculating the multi-channel fit.

The brightest spurious sources revealed by the grid search are tabulated in Table 4. The figures reveal

significant improvement in dynamic range for the full NRM data cube as compared to the single channel case. In both zones, the strongest spurious signal was suppressed by a factor of 3–4 by including 20 channels spanning 1.16 μm to 1.73 μm, ultimately achieving a floor of contrast ratio 64:1 in the outer zone. For reference, in the case of direct AO-corrected imaging with the PHARO camera on the Hale Telescope, Metchev measured a 4σ detection limit of 10:1 at $2\lambda/D$ separation in K_s-band.[60]

We emphasize that the dynamic range enhancement shown in Table 4 is not due to simply compounding the signal-to-noise ratio by summing data across cube channels. The spurious model solutions that set the noise floor are caused by systematic errors rather than signal strength-determined measurement scatter. It is the wavelength diversity enabled the IFS that enables us to reduce their influence.

6. DISCUSSION OF ERROR SOURCES

Although we find that the wavelength dimension provided by the IFS improves the dynamic range of our NRM data, our contrast limit remains over one order of magnitude worse than the best performance of AO-assisted aperture mask observations published to date.[26,29] We attribute this largely to uncalibrated systematic closure phase errors. Earlier, when we considered the fit residuals of the binary star β CrB model, we found that in the 1.58 μm channel (one with relatively high signal-to-noise ratio) there were 15 closure phases with residuals above 10 degrees, and when they were excluded from the fit the RMS across all the residuals was still 4.5 degrees. By comparison, Hinkley et al.[29] controlled these errors to under one degree.

There are two main categories of systematic errors we can imagine in our experiment: those originating from the instrument, and those introduced during the data extraction. On the instrument side there is potential corruption of closure phases from optical misalignments and aberrations. In particular, closure phases are sensitive to wave front errors that deviate from simple pupil-plane 'piston' phase patterns matched to the mask subapertures. We carried out Fresnel diffraction simulations with PROPER, the IDL software package created by J. Krist,[61] to examine the influence of these effects.

First we considered the effect of the pupil mask inclination, one of the problems we noticed in our data. In a PROPER simulation we tested the closure phase accuracy of a simple three-hole mask. We set the geometric scale of the pupil mask and the focal length of the focusing optic (600 mm) to be the same as in our instrument. We found that for a perfect, on-axis, monochromatic ($\lambda = 1.6$ μm) wave front, the closure phase deviates less than half a degree from zero for a mask inclination as high as 15 degrees. Similarly, shifting the entire mask by several millimeters along the optical axis produced no significant closure error. Therefore, we do not consider mask alignment to be a major systematic noise source in our instrument.

Using the same model in PROPER, we tested the effect of phase and amplitude aberrations. We found that a Zernike phase mode of defocus alone, up to a realistic magnitude (0.25 μm), had negligible effect on the closure error. However, when combined with amplitude gradients of order 20% across each mask subaperture, a defocus mode of scale 0.25 μm generates a 2-degree closure error. Since amplitude gradients alone contributed no errors, it appears that the combination of phase and amplitude aberrations, at levels plausible in an AO-corrected beam, can mutually reinforce to produce significant closure errors.

Due to the numerous steps required to extract data from the focal plane image of an integral field spectrograph, we must contend with error sources that exist in neither conventional imaging nor spectroscopy. Several of these were described by Zimmerman et al.[49] For the case of closure phase measurement, our accuracy depends on the ability to discriminate the position and spatial frequencies of the fringes composing the interferogram. Cross-talk is one of the error sources that directly degrades this measurement, by confusing the fringe signals from different baseline and wavelength combinations. While we have mitigated the effect of cross-talk on visibility extraction to a large extent, for some closure triangles we would expect it to remain a concern.

7. CONCLUSIONS

We have carried out the first observation combining non-redundant aperture mask (NRM) interferometry with integral field spectroscopy. The added wavelength dimension of our closure phase data set enabled us to retrieve

the low-resolution near-infrared spectrum of the F-dwarf secondary component of β CrB, a well-studied spectroscopic binary star. To our knowledge, such an accurate spectrum retrieval of a stellar companion at $\sim 2\lambda/D$ angular separation has not been demonstrated before.

Special care was taken to mitigate systematic error sources unique to closely packed IFS data, such as cross-talk between neighboring focal plane spectra. Despite our efforts, relatively large residual errors remained in our β CrB binary model fit ($\sim$9 degrees RMS across all closure triangles and channels). Nevertheless, we did confirm an anticipated boost in contrast limits for spectrally-resolved closure phase data set as compared to a single filter observation. In our case this improvement reduces the noise floor down by a factor of 3–4 at angular separations between $0.5\lambda/D$ and $2.5\lambda/D$. Future experiments are needed to determine if NRM observers can take advantage of this enhancement without suffering from net losses in sensitivity due to the complex noise properties of IFS data.

Our demonstration of a spectrally resolved closure phase data set is relevant to several integral field spectrographs that are planned for extreme adaptive optics. The Gemini Planet Imager (GPI) and the Spectro-Polarimeteric High contrast Exoplanet REsearch (SPHERE) project are equipped to carry out similar kinds of observations.

8. ACKNOWLEDGMENTS

We thank Lewis C. Roberts, Jr. for his assistance in computing the ephemeris of β CrB. We are grateful for support from the National Science Foundation, which enabled us to carry out this experiment through grant AST-0804417. Further support was provided by NASA grant 08-APRA08-0117, and the STScI Director's Discretionary Research Fund. Part of this work was performed under a contract with the California Institute of Technology (Caltech) funded by NASA through the Sagan Fellowship Program. In addition, this work has been partially supported by the National Science Foundation Science and Technology Center for Adaptive Optics, managed by the University of California at Santa Cruz under cooperative agreement AST 98-76783. The Project 1640 team is grateful for support from the Cordelia Corporation, Hilary and Ethel Lipsitz, the Vincent Astor Fund, Judy Vale, and the Plymouth Hill Foundation.

REFERENCES

1. Baldwin, J. E., Haniff, C. A., Mackay, C. D., and Warner, P. J., "Closure phase in high-resolution optical imaging," *Nature* **320**, 595–597 (Apr. 1986).
2. Haniff, C. A., Mackay, C. D., Titterington, D. J., Sivia, D., and Baldwin, J. E., "The first images from optical aperture synthesis," *Nature* **328**, 694–696 (Aug. 1987).
3. Readhead, A. C. S., Nakajima, T. S., Pearson, T. J., Neugebauer, G., Oke, J. B., and Sargent, W. L. W., "Diffraction-limited imaging with ground-based optical telescopes," *AJ* **95**, 1278–1296 (Apr. 1988).
4. Tuthill, P. G., Monnier, J. D., Danchi, W. C., Wishnow, E. H., and Haniff, C. A., "Michelson Interferometry with the Keck I Telescope," *PASP* **112**, 555–565 (Apr. 2000).
5. Racine, R., Walker, G. A. H., Nadeau, D., Doyon, R., and Marois, C., "Speckle Noise and the Detection of Faint Companions," *PASP* **111**, 587–594 (May 1999).
6. Sivaramakrishnan, A., Lloyd, J. P., Hodge, P. E., and Macintosh, B. A., "Speckle Decorrelation and Dynamic Range in Speckle Noise-limited Imaging," *ApJL* **581**, L59–L62 (Dec. 2002).
7. Jennison, R. C., "A phase sensitive interferometer technique for the measurement of the Fourier transforms of spatial brightness distributions of small angular extent," *MNRAS* **118**, 276–+ (1958).
8. Monnier, J. D., Tuthill, P. G., and Danchi, W. C., "Pinwheel Nebula around WR 98A," *ApJL* **525**, L97–L100 (Nov. 1999).
9. Tuthill, P. G., Danchi, W. C., Hale, D. S., Monnier, J. D., and Townes, C. H., "Near- and Mid-Infrared Subarcsecond Structure of the Dusty Symbiotic Star R Aquarii," *ApJ* **534**, 907–914 (May 2000).
10. Tuthill, P., Monnier, J., Tanner, A., Figer, D., Ghez, A., and Danchi, W., "Pinwheels in the Quintuplet Cluster," *Science* **313**, 935–+ (Aug. 2006).
11. Ireland, M. J., Monnier, J. D., Tuthill, P. G., Cohen, R. W., De Buizer, J. M., Packham, C., Ciardi, D., Hayward, T., and Lloyd, J. P., "Born-Again Protoplanetary Disk around Mira B," *ApJ* **662**, 651–657 (June 2007).
12. Leconte, J., Soummer, R., Hinkley, S., Oppenheimer, B. R., Sivaramakrishnan, A., Brenner, D., Kuhn, J., Lloyd, J. P., Perrin, M. D., Makidon, R., Roberts, Jr., L. C., Graham, J. R., Simon, M., Brown, R. A., Zimmerman, N., Chabrier, G., and Baraffe, I., "The Lyot Project Direct Imaging Survey of Substellar Companions: Statistical Analysis and Information from Nondetections," *ApJ* **716**, 1551–1565 (June 2010).
13. Hartung, M., Blanc, A., Fusco, T., Lacombe, F., Mugnier, L. M., Rousset, G., and Lenzen, R., "Calibration of NAOS and CONICA static aberrations. Experimental results," *Astronomy and Astrophysics* **399**, 385–394 (Feb. 2003).
14. Perrin, M. D., Sivaramakrishnan, A., Makidon, R. B., Oppenheimer, B. R., and Graham, J. R., "The Structure of High Strehl Ratio Point-Spread Functions," *ApJ* **596**, 702–712 (Oct. 2003).
15. Marois, C., Doyon, R., Nadeau, D., Racine, R., Riopel, M., Vallée, P., and Lafrenière, D., "TRIDENT: An Infrared Differential Imaging Camera Optimized for the Detection of Methanated Substellar Companions," *PASP* **117**, 745–756 (July 2005).
16. Hinkley, S., Oppenheimer, B. R., Soummer, R., Sivaramakrishnan, A., Roberts, Jr., L. C., Kuhn, J., Makidon, R. B., Perrin, M. D., Lloyd, J. P., Kratter, K., and Brenner, D., "Temporal Evolution of Coronagraphic Dynamic Range and Constraints on Companions to Vega," *ApJ* **654**, 633–640 (Jan. 2007).
17. Tuthill, P., Lloyd, J., Ireland, M., Martinache, F., Monnier, J., Woodruff, H., ten Brummelaar, T., Turner, N., and Townes, C., "Sparse-aperture adaptive optics," in [*Society of Photo-Optical Instrumentation Engineers (SPIE) Conference Series*], *Society of Photo-Optical Instrumentation Engineers (SPIE) Conference Series* **6272** (July 2006).
18. Lloyd, J. P., Martinache, F., Ireland, M. J., Monnier, J. D., Pravdo, S. H., Shaklan, S. B., and Tuthill, P. G., "Direct Detection of the Brown Dwarf GJ 802B with Adaptive Optics Masking Interferometry," *ApJL* **650**, L131–L134 (Oct. 2006).
19. Pravdo, S. H., Shaklan, S. B., Wiktorowicz, S. J., Kulkarni, S., Lloyd, J. P., Martinache, F., Tuthill, P. G., and Ireland, M. J., "Masses of Astrometrically Discovered and Imaged Binaries: G78-28AB and GJ 231.1BC," *ApJ* **649**, 389–398 (Sept. 2006).
20. Sivaramakrishnan, A., Koresko, C. D., Makidon, R. B., Berkefeld, T., and Kuchner, M. J., "Ground-based Coronagraphy with High-order Adaptive Optics," *ApJ* **552**, 397–408 (May 2001).

21. Soummer, R., "Apodized Pupil Lyot Coronagraphs for Arbitrary Telescope Apertures," *ApJL* **618**, L161–L164 (Jan. 2005).
22. Sivaramakrishnan, A. and Lloyd, J. P., "Spiders in Lyot Coronagraphs," *ApJ* **633**, 528–533 (Nov. 2005).
23. Chauvin, G., Lagrange, A.-M., Bonavita, M., Zuckerman, B., Dumas, C., Bessell, M. S., Beuzit, J.-L., Bonnefoy, M., Desidera, S., Farihi, J., Lowrance, P., Mouillet, D., and Song, I., "Deep imaging survey of young, nearby austral stars . VLT/NACO near-infrared Lyot-coronographic observations," *Astronomy and Astrophysics* **509**, A52+ (Jan. 2010).
24. Ireland, M. J., Kraus, A., Martinache, F., Lloyd, J. P., and Tuthill, P. G., "Dynamical Mass of GJ 802B: A Brown Dwarf in a Triple System," *ApJ* **678**, 463–471 (May 2008).
25. Martinache, F., Rojas-Ayala, B., Ireland, M. J., Lloyd, J. P., and Tuthill, P. G., "Visual Orbit of the Low-Mass Binary GJ 164 AB," *ApJ* **695**, 1183–1190 (Apr. 2009).
26. Kraus, A. L., Ireland, M. J., Martinache, F., and Lloyd, J. P., "Mapping the Shores of the Brown Dwarf Desert. I. Upper Scorpius," *ApJ* **679**, 762–782 (May 2008).
27. Bernat, D., Bouchez, A. H., Ireland, M., Tuthill, P., Martinache, F., Angione, J., Burruss, R. S., Cromer, J. L., Dekany, R. G., Guiwits, S. R., Henning, J. R., Hickey, J., Kibblewhite, E., McKenna, D. L., Moore, A. M., Petrie, H. L., Roberts, J., Shelton, J. C., Thicksten, R. P., Trinh, T., Tripathi, R., Troy, M., Truong, T., Velur, V., and Lloyd, J. P., "A Close Companion Search Around L Dwarfs Using Aperture Masking Interferometry and Palomar Laser Guide Star Adaptive Optics," *ApJ* **715**, 724–735 (June 2010).
28. Dekany, R. G., Wallace, J. K., Brack, G., Oppenheimer, B. R., and Palmer, D., "Initial test results from the Palomar 200-in. adaptive optics system [3126-33]," in [*Society of Photo-Optical Instrumentation Engineers (SPIE) Conference Series*], R. K. Tyson & R. Q. Fugate, ed., *Society of Photo-Optical Instrumentation Engineers (SPIE) Conference Series* **3126**, 269–+ (Oct. 1997).
29. Hinkley, S., Carpenter, J. M., Ireland, M. J., and Kraus, A. L., "Observational Constraints on Companions Inside of 10 AU in the HR 8799 Planetary System," *ApJL* **730**, L21+ (Apr. 2011).
30. Marois, C., Macintosh, B., Barman, T., Zuckerman, B., Song, I., Patience, J., Lafrenière, D., and Doyon, R., "Direct Imaging of Multiple Planets Orbiting the Star HR 8799," *Science* **322**, 1348– (Nov. 2008).
31. Metchev, S., Marois, C., and Zuckerman, B., "Pre-Discovery 2007 Image of the HR 8799 Planetary System," *ApJL* **705**, L204–L207 (Nov. 2009).
32. Marois, C., Zuckerman, B., Konopacky, Q. M., Macintosh, B., and Barman, T., "Images of a fourth planet orbiting HR 8799," *Nature* **468**, 1080–1083 (Dec. 2010).
33. Soummer, R., Brendan Hagan, J., Pueyo, L., Thormann, A., Rajan, A., and Marois, C., "Orbital Motion of HR 8799 b, c, d Using Hubble Space Telescope Data from 1998: Constraints on Inclination, Eccentricity, and Stability," *ApJ* **741**, 55 (Nov. 2011).
34. Huélamo, N., Lacour, S., Tuthill, P., Ireland, M., Kraus, A., and Chauvin, G., "A companion candidate in the gap of the T Chamaeleontis transitional disk," *Astronomy and Astrophysics* **528**, L7 (Apr. 2011).
35. Kraus, A. L. and Ireland, M. J., "LkCa 15: A Young Exoplanet Caught at Formation?," *ApJ* **745**, 5 (Jan. 2012).
36. Biller, B., Lacour, S., Juhász, A., Benisty, M., Chauvin, G., Olofsson, J., Pott, J.-U., Müller, A., Sicilia-Aguilar, A., Bonnefoy, M., Tuthill, P., Thebault, P., Henning, T., and Crida, A., "A Likely Close-In Low-Mass Stellar Companion to the Transitional Disk Star HD 142527," *ArXiv e-prints* (June 2012).
37. Hinkley, S., Oppenheimer, B. R., Zimmerman, N., Brenner, D., Parry, I. R., Crepp, J. R., Vasisht, G., Ligon, E., King, D., Soummer, R., Sivaramakrishnan, A., Beichman, C., Shao, M., Roberts, L. C., Bouchez, A., Dekany, R., Pueyo, L., Roberts, J. E., Lockhart, T., Zhai, C., Shelton, C., and Burruss, R., "A New High Contrast Imaging Program at Palomar Observatory," *PASP* **123**, 74–86 (Jan. 2011).
38. Bacon, R., Adam, G., Baranne, A., Courtès, G., Dubet, D., Dubois, J.-P., Georgelin, Y., Monnet, G., Pecontal, E., and Urios, J., "The Integral Field Spectrograph TIGER," in [*European Southern Observatory Conference and Workshop Proceedings*], M.-H. Ulrich, ed., *European Southern Observatory Conference and Workshop Proceedings* **30**, 1185–+ (1988).
39. Bacon, R., Adam, G., Baranne, A., Courtes, G., Dubet, D., Dubois, J. P., Emsellem, E., Ferruit, P., Georgelin, Y., Monnet, G., Pecontal, E., Rousset, A., and Say, F., "3D spectrography at high spatial resolution. I. Concept and realization of the integral field spectrograph TIGER.," *Astronomy and Astrophysics, Supplement* **113**, 347–+ (Oct. 1995).

40. Sparks, W. B. and Ford, H. C., "Imaging Spectroscopy for Extrasolar Planet Detection," *ApJ* **578**, 543–564 (Oct. 2002).
41. Crepp, J. R., Pueyo, L., Brenner, D., Oppenheimer, B. R., Zimmerman, N., Hinkley, S., Parry, I., King, D., Vasisht, G., Beichman, C., Hillenbrand, L., Dekany, R., Shao, M., Burruss, R., Roberts, L. C., Bouchez, A., Roberts, J., and Soummer, R., "Speckle Suppression with the Project 1640 Integral Field Spectrograph," *ApJ* **729**, 132–+ (Mar. 2011).
42. Zimmerman, N., Oppenheimer, B. R., Hinkley, S., Brenner, D., Parry, I. R., Sivaramakrishnan, A., Hillenbrand, L., Beichman, C., Crepp, J. R., Vasisht, G., Roberts, L. C., Burruss, R., King, D. L., Soummer, R., Dekany, R., Shao, M., Bouchez, A., Roberts, J. E., and Hunt, S., "Parallactic Motion for Companion Discovery: An M-Dwarf Orbiting Alcor," *ApJ* **709**, 733–740 (Feb. 2010).
43. Hinkley, S., Oppenheimer, B. R., Brenner, D., Zimmerman, N., Roberts, L. C., Parry, I. R., Soummer, R., Sivaramakrishnan, A., Simon, M., Perrin, M. D., King, D. L., Lloyd, J. P., Bouchez, A., Roberts, J. E., Dekany, R., Beichman, C., Hillenbrand, L., Burruss, R., Shao, M., and Vasisht, G., "Discovery and Characterization of a Faint Stellar Companion to the A3V Star ζ Virginis," *ApJ* **712**, 421–428 (Mar. 2010).
44. Monnier, J. D., "Optical interferometry in astronomy," *Reports on Progress in Physics* **66**, 789–857 (May 2003).
45. Perryman, M. A. C., Lindegren, L., Kovalevsky, J., Hoeg, E., Bastian, U., Bernacca, P. L., Crézé, M., Donati, F., Grenon, M., van Leeuwen, F., van der Marel, H., Mignard, F., Murray, C. A., Le Poole, R. S., Schrijver, H., Turon, C., Arenou, F., Froeschlé, M., and Petersen, C. S., "The HIPPARCOS Catalogue," *Astronomy and Astrophysics* **323**, L49–L52 (July 1997).
46. Oetken, L. and Orwert, R., "The binary nature of the magnetic star Beta CrB," *Astronomische Nachrichten* **305**, 317–323 (1984).
47. Campbell, W. W. and Moore, J. H., "A List of Six Stars whose Radial Velocities Vary," *Lick Observatory Bulletin* **4**, 161–162 (1907).
48. Muterspaugh, M. W., Hartkopf, W. I., Lane, B. F., O'Connell, J., Williamson, M., Kulkarni, S. R., Konacki, M., Burke, B. F., Colavita, M. M., Shao, M., and Wiktorowicz, S. J., "The Phases Differential Astrometry Data Archive. II. Updated Binary Star Orbits and a Long Period Eclipsing Binary," *AJ* **140**, 1623–1630 (Dec. 2010).
49. Zimmerman, N., Brenner, D., Oppenheimer, B. R., Parry, I. R., Hinkley, S., Hunt, S., and Roberts, R., "A Data-Cube Extraction Pipeline for a Coronagraphic Integral Field Spectrograph," *PASP* **123**, 746–763 (June 2011).
50. Johnson, J. A., Marcy, G. W., Fischer, D. A., Wright, J. T., Reffert, S., Kregenow, J. M., Williams, P. K. G., and Peek, K. M. G., "Retired A Stars and Their Companions. II. Jovian planets orbiting κ CrB and HD 167042," *ApJ* **675**, 784–789 (Mar. 2008).
51. Bowler, B. P., Johnson, J. A., Marcy, G. W., Henry, G. W., Peek, K. M. G., Fischer, D. A., Clubb, K. I., Liu, M. C., Reffert, S., Schwab, C., and Lowe, T. B., "Retired A Stars and Their Companions. III. Comparing the Mass-Period Distributions of Planets Around A-Type Stars and Sun-Like Stars," *ApJ* **709**, 396–410 (Jan. 2010).
52. Baraffe, I., Chabrier, G., Barman, T. S., Allard, F., and Hauschildt, P. H., "Evolutionary models for cool brown dwarfs and extrasolar giant planets. The case of HD 209458," *Astronomy and Astrophysics* **402**, 701–712 (May 2003).
53. Sivia, D. S., [*Data Analysis: A Bayesian Tutorial*], Oxford Science Publications (2006).
54. Bruntt, H., Kervella, P., Mérand, A., Brandão, I. M., Bedding, T. R., Ten Brummelaar, T. A., Coudé Du Foresto, V., Cunha, M. S., Farrington, C., Goldfinger, P. J., Kiss, L. L., McAlister, H. A., Ridgway, S. T., Sturmann, J., Sturmann, L., Turner, N., and Tuthill, P. G., "The radius and effective temperature of the binary Ap star β CrB from CHARA/FLUOR and VLT/NACO observations," *Astronomy and Astrophysics* **512**, A55+ (Mar. 2010).
55. Tokovinin, A. A., "Interferometer orbits for seven binaries," *Pis ma Astronomicheskii Zhurnal* **10**, 293–296 (Apr. 1984).
56. Rayner, J. T., Cushing, M. C., and Vacca, W. D., "The Infrared Telescope Facility (IRTF) Spectral Library: Cool Stars," *ApJS* **185**, 289–432 (Dec. 2009).

57. Pickles, A. J., "A Stellar Spectral Flux Library: 1150-25000 Å," *PASP* **110**, 863–878 (July 1998).
58. Gray, R. O., Graham, P. W., and Hoyt, S. R., "The Physical Basis of Luminosity Classification in the Late A-, F-, and Early G-Type Stars. II. Basic Parameters of Program Stars and the Role of Microturbulence," *AJ* **121**, 2159–2172 (Apr. 2001).
59. Ireland, M. J., Monnier, J. D., and Thureau, N., "Monte-Carlo imaging for optical interferometry," in [*Society of Photo-Optical Instrumentation Engineers (SPIE) Conference Series*], *Society of Photo-Optical Instrumentation Engineers (SPIE) Conference Series* **6268** (July 2006).
60. Metchev, S. A. and Hillenbrand, L. A., "The Palomar/Keck Adaptive Optics Survey of Young Solar Analogs: Evidence for a Universal Companion Mass Function," *ApJS* **181**, 62–109 (Mar. 2009).
61. Krist, J. E., "PROPER: an optical propagation library for IDL," in [*Society of Photo-Optical Instrumentation Engineers (SPIE) Conference Series*], *Society of Photo-Optical Instrumentation Engineers (SPIE) Conference Series* **6675** (Sept. 2007).